Proceedings of the 7th International Conference on Computing and Data Science
DOI: 10.54254/2755-2721/2025.26140

Discussion on the Algorithm for Determining the Optimal Rod Length of a Five Link Closed Chain Double Wheel Leg Robot

Zihan Cen

College of Automation, Nanjing University of Science and Technology, Nanjing, China
3294277501@qq.com

Abstract. This paper proposes a novel obstacle-crossing method for wheeled bipedal robots with specialized leg configurations, addressing the limitations of existing jumping-based approaches that suffer from high landing impacts, suboptimal jump heights, and extreme demands on joint torque/battery discharge. Experimenter first derive the robot's dynamics model and establish an Obstacle-Climbing Wheeled Inverted Pendulum (OCWIP) model corresponding to the asymmetric five-bar linkage mechanism, replacing spring forces with virtual forces. Trajectory planning synchronized with body-wheel motion is then implemented based on the OCWIP model, dividing obstacle-crossing into three phases for dynamic analysis. Compared to jumping methods, our approach utilizes passive body tilting followed by leg retraction to ascend steps, significantly reducing mechanical shock on leg structures and extending the lifespan of actuators/batteries. A hierarchical controller integrates leg motion, aerial attitude adjustment, and trajectory tracking to achieve real-time stabilization and robust execution. Experimental validation demonstrates >90% success rate on a physical platform. Key contributions are: 1) A GPU-accelerated solver for optimal linkage combination; 2) Development of the asymmetric five-bar OCWIP model; 3) Hardware validation of the obstacle-crossing framework.

Keywords: Obstacle negotiation, Hierarchical control, Wheel-legged robots, Asymmetric five-bar linkage

1. Introduction

The field of wheeled bipedal robot balance control continues to advance, with several notable platforms emerging globally. Ascento,a compact wheeled bipedal robot developed by ETH Zurich in Switzerland [1,2]. Handle [3], a robot from Boston. researchers at China's Harbin Institute of Technology developed robot WLR [4], WLRII [5,6]. However, their obstacle-crossing capabilities remain limited . Jumping serves as the mainstream solution but suffers from substantial landing impacts, suboptimal jump heights, and stringent demands on joint motor torque and battery discharge capacity .

This research presents a new method for wheeled robots to cross obstacles. The method is designed for robots with specific structural features. Initially, experimenter establish a

DOI: 10.54254/2755-2721/2025.26140

comprehensive dynamics model for a wheeled bipedal robot, developing an inverted swing model termed Obstacle-Climbing Wheeled Inverted Pendulum (OCWIP) model that corresponds to an asymmetric five-bar coupling mechanism within the robotic leg assembly. Unlike traditional spring-loaded inverted pendulum models, the OCWIP framework uses virtual force fields instead of mechanical springs. These force fields are calculated computationally. Next, obstacle navigation trajectories are systematically planned using this model, synchronizing the motion between the robot's main body and wheels to fully exploit its kinematic potential. The obstacle negotiation process is segmented into three distinct operational phases, with each phase subjected to rigorous dynamic modeling and analysis via the OCWIP system.

The new strategy exhibits fundamental differences compared to methods reliant on jumping. Jumping approaches generate substantial impact stresses during the landing phase. These methods also require very high torque levels and considerable battery power. In contrast, the new strategy utilizes a passive body tilting mechanism. This tilting action is followed by coordinated leg retraction. Together, these actions enable obstacle ascent. This methodology significantly reduces mechanical impacts imposed on leg structures. Consequently, it extends the service life of joint actuators.

2. System introduction

This research describes a six-degree-of-freedom (6-DoF) wheeled bipedal robot design. (Figure 1.) The robot has a total mass of 5.9 kilograms. Its control system uses a dual-layer architecture. A low-level motion control board handles basic locomotion and communication with an upper computer. The upper computer manages motion planning and high-level decisions. Power comes from a single battery pack. This battery supports around one hour of continuous operation. Leg movement is powered by brushless DC (BLDC) motors. Wheel motion is driven by BLDC motors with custom reducers. To replace the original P18 units , experimenter changed the reduction ratio to 15.6:1.

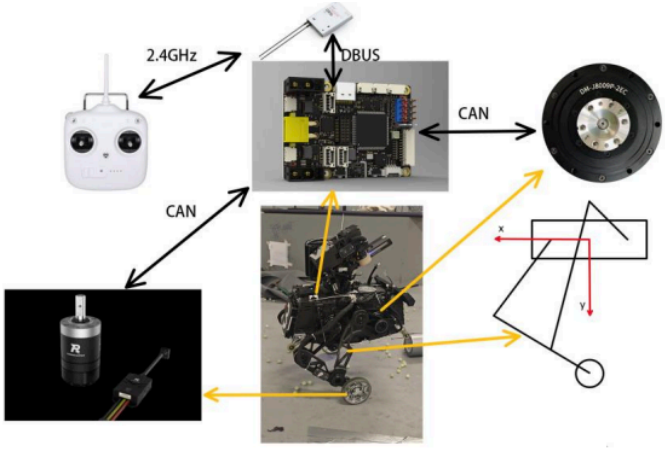

Figure 1. Robot hardware systems

The leg assembly uses an asymmetrical five-bar linkage mechanism. This design works better than symmetrical five-bar linkages or simpler four-bar designs. The asymmetry helps the robot adapt to real-world terrain like steps and staircases. Also, it gives more kinematic freedom than a four-bar linkage, so it improves postural stability during stance and movement. A key problem with symmetric five-bar linkages happens during step negotiation: interference often occurs between the linkage near the step edge and the step itself. This interference physically stops the robot from tilting

DOI: 10.54254/2755-2721/2025.26140

its body or retracting the leg enough to clear the obstacle. Jumping could be an alternative, but this needs very high joint motor peak torque and battery power, and it increases the risk of mechanical failure . But the wheeled bipedal robot with the asymmetrical five-bar linkage, because of its larger motion range, can climb steps by a specific method. It first makes wheel contact with the step surface, then retracts the leg along carefully planned paths. This avoids the risks linked to jumping. Therefore, using the asymmetrical five-bar linkage for obstacle negotiation shows big practical advantages. Compared to symmetrical designs, it offers better operational safety and mechanical feasibility.

3. Optimal linkage length algorithm

The symmetric five-link configuration exhibits limitations in obstacle negotiation due to its insufficient effective workspace. To address this, a novel asymmetric configuration is proposed, which reduces motor torque load while ensuring a larger operational range. The solution approach consists of three stages: generating link-length combinations, screening based on end-effector motion point clouds, and further refinement via Virtual Motion Control (VMC) simulations to evaluate motor loads under identical payload conditions. As depicted in the schematic, the five-link mechanism parameters define two motor-driven revolute joints with angles measurable via encoders. The control task primarily focuses on the position of point F at the mechanism's end-effector. (Figure 2.)

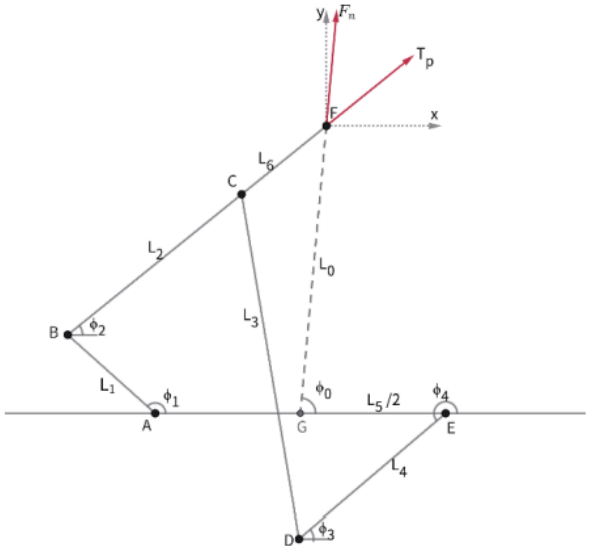

Figure 2. Parameter definition of asymmetric five bar linkage

For this system, the mapping relationship between the end-effector thrust F_n and central-axis torque T_p (corresponding to polar coordinates L_0, ϕ_0) and the driving motor torques T_1, T_4 must be established. Defining x= $[L_0, \phi_0]^T$, $q = [\phi_1, \phi_4]^T$, the full differential of the forward kinematics $x = f(q)$ yields:

$$\begin{bmatrix} T_1 \\ T_4 \end{bmatrix} = J^T R M \begin{bmatrix} F_n \\ T_p \end{bmatrix} \tag{1}$$

where the rotation matrix

DOI: 10.54254/2755-2721/2025.26140

$$R = \begin{bmatrix} cos(\phi_o - \pi/2) & -sin(\phi_o - \pi/2) \\ sin(\phi_o - \pi/2) & cos(\phi_o - \pi/2) \end{bmatrix} \tag{2}$$

and transformation matrix M= $\begin{bmatrix} 0 & -1/l_0 \\ 1 & 0 \end{bmatrix}$.

The final torque mapping is expressed as:

$$\begin{bmatrix} T_1 \\ T_4 \end{bmatrix} = \begin{pmatrix} -\frac{l_1 sin(\sigma_2+\sigma_3) sin(\varphi_1-\sigma_4)}{sin(\sigma_4+\sigma_3)} & -\frac{l_1 cos(\sigma_2+\sigma_3) sin(\varphi_1-\sigma_4)}{\sigma_1} \\ \frac{l_4 sin(\varphi_4+\sigma_3) sin(\sigma_2-\sigma_4)}{sin(\sigma_4+\sigma_3)} & \frac{l_4 sin(\varphi_4+\sigma_3) cos(\sigma_2-\sigma_4)}{\sigma_1} \end{pmatrix} \begin{bmatrix} F_n \\ T_p \end{bmatrix} \tag{3}$$

$$where$$

$$\sigma_1 = sin(\sigma_4+\sigma_3)\sqrt{\left(\frac{l_5}{2} + \frac{l_6(l_5+l_4 cos(\varphi_4))}{l_3} - \frac{(l_3+l_6)(l_2 cos(\sigma_4)+l_1 cos(\varphi_1))}{l_3}\right)^2 + \left(\frac{(l_3+l_6)(l_2 sin(\sigma_4)+l_1 sin(\varphi_1))}{l_3} - \frac{l_4 l_6 sin(\varphi_4)}{l_3}\right)^2}$$

$$\sigma_2 = atan2\left(\frac{(l_3+l_6)(l_2 sin(\sigma_4)+l_1 sin(\varphi_1))}{l_3} - \frac{l_4 l_6 sin(\varphi_4)}{l_3}, \frac{(l_3+l_6)(l_2 cos(\sigma_4)+l_1 cos(\varphi_1))}{l_3} - \frac{l_6(l_5+l_4 cos(\varphi_4))}{l_3} - \frac{l_5}{2}\right)$$

$$\sigma_3 = atan\left(\frac{l_2 sin(\sigma_4)+l_1 sin(\varphi_1)-l_4 sin(\varphi_4)}{l_5-l_2 cos(\sigma_4)-l_1 cos(\varphi_1)+l_4 cos(\varphi_4)}\right)$$

$$\sigma_4 = 2atan\left(\frac{\sqrt{4{l_2}^2\sigma_6 - \left(\sigma_6+\sigma_5+{l_2}^2-{l_3}^2\right)^2 + 4{l_2}^2\sigma_5} - 2l_2(l_1 sin(\varphi_1)-l_4 sin(\varphi_4))}{\sigma_6+\sigma_5+{l_2}^2-{l_3}^2+2l_2(l_5-l_1 cos(\varphi_1)+l_4 cos(\varphi_4))}\right)$$

$$\sigma_5 = (l_5 - l_1 cos(\varphi_1) + l_4 cos(\varphi_4))^2$$

$$\sigma_6 = (l_1 sin(\varphi_1) - l_4 sin(\varphi_4))^2$$

The effective end-effector workspace is defined as a 135° annular sector with radii 130–350 mm centered on the joint axes (Figure. 3). Point clouds within this domain are discretized into polygonal cells for area calculation. Link-length combinations achieving >85% workspace coverage (area > 7.0497 dm^2) undergo secondary screening. For each qualifying combination, VMC computes motor torques across all workspace points. The optimal set minimizes the weighted sum of absolute motor torques under varied loads and positions. The resulting parameters are: $L1 = 152.5,\ L2 = 160,\ L3 = 250,\ L4 = 90,\ L5 = 170,\ L6 = 100.\,(mm)$.

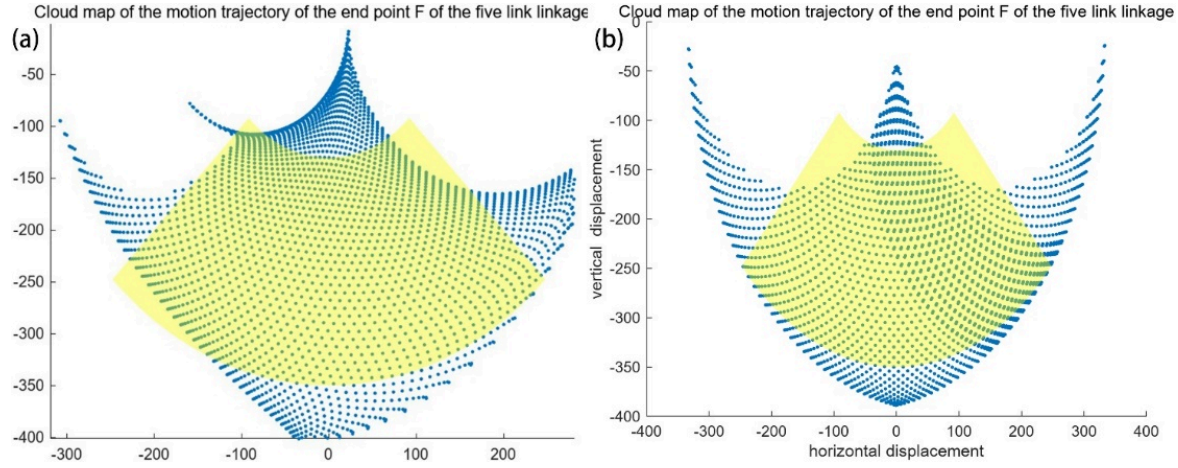

Figure 3. (a) Asymmetric five-bar linkage end point cloud trajectory (b) Symmetric five-bar linkage end point cloud trajectory

DOI: 10.54254/2755-2721/2025.26140

Comparative analysis reveals the asymmetric configuration's workspace area (7.5551 dm²) exceeds the symmetric counterpart (6.2030 dm²) at similar leg extension ranges, with higher point-cloud density in the operational zone. Under identical payloads within the effective workspace, motor torque analysis (Figure. 4) confirms the asymmetric design achieves both lower magnitude and more uniform torque distribution.

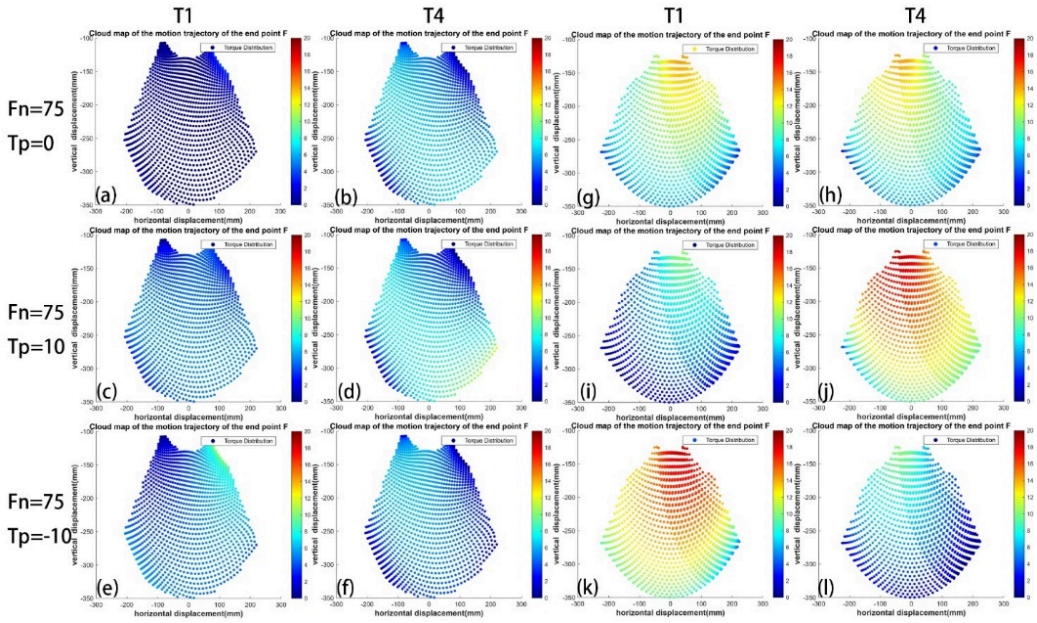

Figure 4. Point cloud and load of end effective region (load size is indicated by color) (a)~(f) asymmetric five bar linkage (g)~(l) symmetric five bar linkage

4. Dynamic modeling

In whole-body modeling, the robot is simplified into a five-component rigid-body system, comprising the main body, left leg, right leg, left drive wheel, and right drive wheel. The legs are modeled as rigid elements with parameters corresponding to their instantaneous lengths at any given time, and this simplification inherently neglects the potential influence of leg-body configuration changes on the moment of inertia about the z-axis—a common assumption in reduced-order models to mitigate complexity, as parameterized in studies like those involving mass and inertia properties.Consequently, this approach facilitates the formulation and solution of dynamic equations, such as those derived from Lagrangian or Newton-Euler formulations, which efficiently describe system kinematics and kinetics.Such modeling strategies are widely adopted in legged robot research; for instance, in dynamically stable robotic systems, the rigid-body abstraction enables a focused analysis on core dynamic behaviors, as demonstrated in experimental implementations like untethered quadrupedal running [7]. Subsequent paragraph will elaborate on the definitions of relevant variables and systematically derive the associated mathematical formulations(Table 1) [8].

DOI: 10.54254/2755-2721/2025.26140

Table 1. Model variable definition of wheel-legged inverted pendulum

$symbol(i=l,r)$	meaning
$\theta_{l,i}$	Leg inclination angle
θ_b	Body inclination angle
$T_{lw,i}$	Driving wheel torque
$T_{b,i}$	Leg actuation torque
R_w,R_l	Driving wheel radius ,Half-track width
l_i,$l_{w,i}$	leg length ,Distance from wheel to leg CoM
$l_{b,i}$	Distance from leg COM to body COM
m_w,m_l,m_b	Mass of wheel, leg, and body
I_w,I_l,I_b	Rotational inertia of wheel, leg, and body about their CoM

$$
\begin{cases}
\left(I_w\frac{l_l}{R_w}+m_wR_wl_l+m_lR_wl_{b,l}\right)\ddot{\theta}_{w,l}+(m_ll_{w,l}l_{b,l}-I_{l,l})\ddot{\theta}_{l,l}+\left(m_ll_{w,l}+\frac{1}{2}m_bl_l\right)g\theta_{l,l}+T_{bl,l}-T_{lw,l}\left(1+\frac{l_l}{R_w}\right)=0\\
\left(I_w\frac{l_r}{R_w}+m_wR_wl_r+m_lR_wl_{b,r}\right)\ddot{\theta}_{w,r}+(m_ll_{w,r}l_{b,r}-I_{l,r})\ddot{\theta}_{l,r}+\left(m_ll_{w,r}+\frac{1}{2}m_bl_r\right)g\theta_{l,r}+T_{bl,r}-T_{lw,r}\left(1+\frac{l_r}{R_w}\right)=0\\
-\left(m_wR_w^2+I_w+m_lR_w^2+\frac{1}{2}m_bR_w^2\right)\ddot{\theta}_{w,l}-\left(m_wR_w^2+I_w+m_lR_w^2+\frac{1}{2}m_bR_w^2\right)\ddot{\theta}_{w,r}-\left(m_lR_wl_{w,l}+\frac{1}{2}m_bR_wl_l\right)\ddot{\theta}_{l,l}\\
-\left(m_lR_wl_{w,r}+\frac{1}{2}m_bR_wl_r\right)\ddot{\theta}_{l,r}+T_{lw,l}+T_{lw,r}=0\\
\left(m_wR_wl_c+I_w\frac{l_c}{R_w}+m_lR_wl_c\right)\ddot{\theta}_{w,l}+\left(m_wR_wl_c+I_w\frac{l_c}{R_w}+m_lR_wl_c\right)\ddot{\theta}_{w,r}+m_ll_{w,l}l_c\ddot{\theta}_{l,l}+m_ll_{w,r}l_c\ddot{\theta}_{l,r}-I_b\ddot{\theta}_{l,r}\\
+m_bgl_c\theta_b-(T_{lw,l}+T_{lw,r})\frac{l_c}{R_w}-(T_{bl,l}+T_{bl,r})=0\\
\left(\frac{1}{2}I_z\frac{R_w}{R_l}+I_w\frac{R_l}{R_w}\right)\ddot{\theta}_{w,l}-\left(\frac{1}{2}I_z\frac{R_w}{R_l}+I_w\frac{R_l}{R_w}\right)\ddot{\theta}_{w,r}+\frac{1}{2}I_z\frac{l_l}{R_l}\ddot{\theta}_{l,l}-\frac{1}{2}I_z\frac{l_r}{R_l}\ddot{\theta}_{l,r}-T_{lw,l}\frac{R_l}{R_w}+T_{lw,r}\frac{R_l}{R_w}=0
\end{cases}
\tag{4-8}
$$

5. Control strategy

The dynamic modeling equations are linearized using Taylor expansion to establish the state equation as

$$\dot{x}=Ax+Bu \tag{9}$$

where the state vector encompasses position, velocity, and angular displacement/states of the system components: $x=\left[s,\dot{s},\varphi,\dot{\varphi},\theta_{ll},\dot{\theta_{ll}},\theta_{lr},\dot{\theta_{lr}},\theta_b,\dot{\theta_b}\right]^T$

and the input vector$u=[T_{wl},T_{wr},T_{ll},T_{lr}]^T$represents the applied torques. The reference state vector is defined as $x_d=\left[s_d,\dot{s_d},\varphi_d,\dot{\varphi_d},\theta_{lld},\dot{\theta_{lld}},\theta_{lrd},\dot{\theta_{lrd}},\theta_{bd},\dot{\theta_{bd}}\right]^T$.

The matrices A and B are derived from the coupled equations of the dynamic model; due to their complexity and extensive expressions, they are symbolically represented here. The control law employs state feedback $u=-K(x_d-x)$, with the feedback gain matrix K computed via the Linear Quadratic Regulator (LQR) method. This involves minimizing the quadratic cost functional

DOI: 10.54254/2755-2721/2025.26140

$$J = \int_0^\infty (x^T Q x + u^T R u) dt \tag{10}$$

where Q and R are positive semi-definite and positive definite weighting matrices penalizing state deviations and control effort, respectively. The solution to this optimization problem requires solving the Algebraic Riccati Equation (ARE)

$$A^T P + PA - PBR^{-1}B^T P + Q = 0 \tag{11}$$

this process yields the gain matrix

$$K = R^{-1}B^T P \tag{12}$$

The OCWIP model in two distinct modes for the wheel and leg subsystems. During obstacle traversal, the wheel subsystem experiences a sudden reduction in supporting force, approximating a no-load, resistance-free rotation condition. Under such dynamics, continued use of the LQR balance controller would cause the wheels to accelerate uncontrollably towards maximum speed. To mitigate this, the wheel control is switched to a closed-loop proportional velocity control law

$$T_{wl,r} = -k_p (v_d - v) \tag{13}$$

with the desired velocity v_d =0 m/s.

For the leg subsystem, contact with the step is detected via the horizontal force F_x at the end of the linkage. This force is computed from the joint motor output torques T_1 and T_4 using the transformation

$$\begin{bmatrix} F_x \\ F_y \end{bmatrix} = \left(J^T\right)^{-1} \begin{bmatrix} T_1 \\ T_4 \end{bmatrix} \tag{14}$$

where denotes the Jacobian matrix specified in Equation (1). The leg subsystem continues to utilize the LQR-based balance controller for stability. Here, the reference state is set to $x_d = [0,0,0,0,\theta_{leg},0,\theta_{leg},0,\theta_{body},0]$, and by strategically tuning the Q $and R matrices, a retraction trajectory for the leg can be effectively planned during obstacle negotiation .

The obstacle-crossing process involves three key phases. (Figure 5.) At time t_1 , wheel detection of the step triggers a switch to the obstacle-crossing inverted pendulum controller. Subsequently, at time t_2 , once the wheels have successfully surmounted the obstacle, the system reverts to the standard balance posture control to resume normal operation. This mode-switching strategy ensures stability and performance adaptation during the critical transition phases of obstacle traversal.

DOI: 10.54254/2755-2721/2025.26140

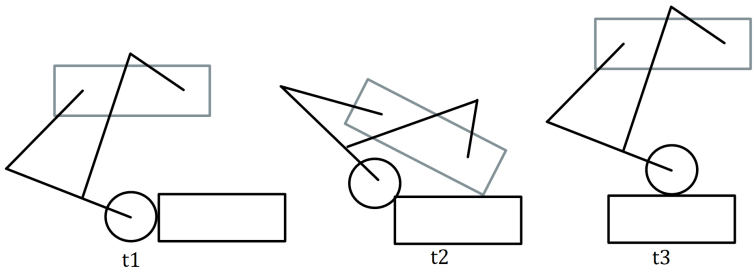

Figure 5. Schematic diagram of robot obstacle climbing process

6. Experiments results

Physical experiments were conducted to verify the obstacle-crossing strategy proposed in this research. This validation work builds on earlier modeling and simulation frameworks . Figure 6 shows the step-by-step process of the robot crossing a step during movement. From phases (a) to (c), the robot moves forward while detecting the edge of the step. This demonstrates proactive sensing of the environment, similar to terrain-scanning behaviors seen in multi-legged robots. At the moment shown in phase (c), the step is recognized. This detection triggers the start of leg retraction.During phases (d) to (g), the robot actively pulls its legs back. It also switches into the OCWIP model control mode. This control mode optimizes limb paths to minimize energy use during elevation. By phase (h), the legs are fully retracted vertically. This marks the end of the clearance action. Following this, in phases (j) to (l), the robot regains static balance. It does this by switching back to the balance control model. This switch confirms the stability recovery mechanism built into the control system.

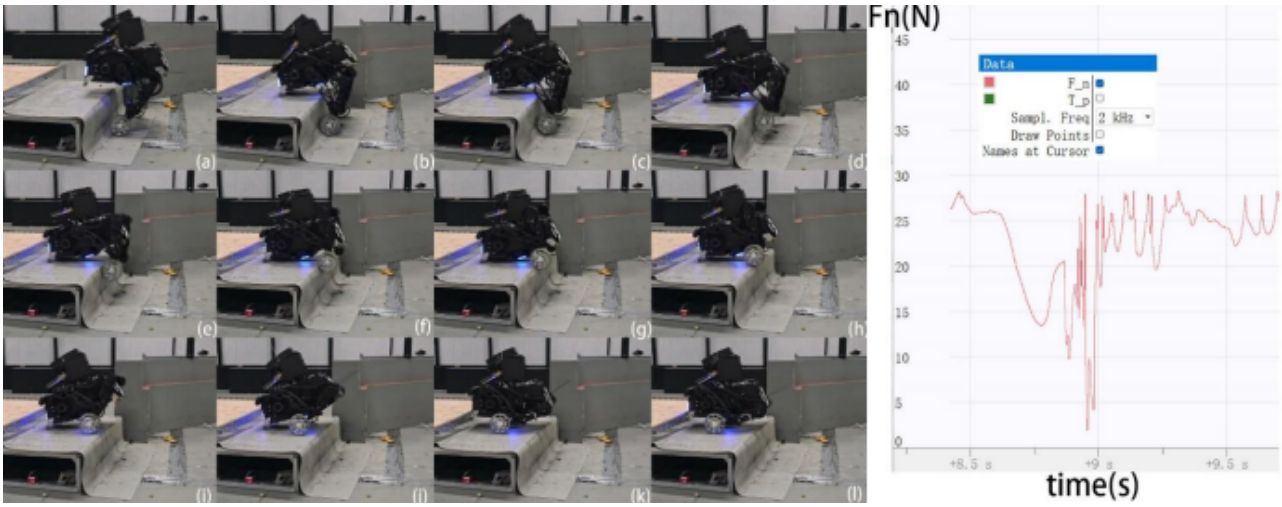

Figure 6. Process diagram of robot obstacle surmounting experiment

Force data from the right panel of Figure 6 show a significant drop in leg support force. The force decreases to 5 N when the step is detected at 8.91 seconds. This reduction happens exactly when the retraction phase begins. It matches the expected unloading dynamics during elevation. Ground contact is re-established at 9.0 seconds. This reconnection allows force to recover quickly. Rapid force recovery enables the stable stance to be restored. Importantly, the highest support forces stay below 30 N throughout the entire process. These force levels are much lower than loads typically

DOI: 10.54254/2755-2721/2025.26140

seen in jumping-actuator systems. This validates the strategy's mechanical efficiency. It also confirms the reduction in stress on the joints.

7. Conclusion

This study introduces a novel obstacle-crossing paradigm for wheeled bipedal robots via the development and experimental validation of the Asymmetric Five-Bar OCWIP model. By replacing spring forces with virtual forces synchronized with wheel-body coordination, the proposed model enables trajectory planning that minimizes landing impacts and joint torque demands—addressing critical limitations of existing Wheeled-Spring-Loaded Inverted Pendulum (W-SLIP) and Nonholonomic Wheeled-Spring-Loaded Inverted Pendulum (NW-SLIP) jumping methods [9]. The hierarchical control architecture effectively harmonizes leg retraction, body tilting, and aerial stabilization, achieving robust real-time performance with >90% success rates in structured environments. While the approach significantly enhances mechanical durability and energy efficiency, its efficacy on highly irregular remains constrained by wheel-ground interaction dynamics . Future work will focus on integrating adaptive traction control and terrain perception modules to expand applicability to unstructured outdoor scenarios. The OCWIP framework, coupled with GPU-accelerated linkage optimization, establishes a foundational methodology for next-generation wheeled bipedal robots prioritizing longevity, efficiency, and dynamic stability in complex navigational tasks.

References

[1] V. Klemm et al., “Ascento: A two-wheeled jumping robot, ” in Proc. Int. Conf. Robot. Automat., 2019, pp. 7515–7521.
[2] V. Klemm et al., “LQR-assisted whole-body control of a wheeled bipedal robot with kinematic loops, ” IEEE Robot. Automat. Lett., vol. 5, no. 2, pp. 3745–3752, Apr. 2020.
[3] Jemin Hwangbo et al., Learning agile and dynamic motor skills for legged robots. Sci. Robot.4, eaau5872(2019).DOI: [10.1126/scirobotics.aau5872]
[4] X. Li et al., “Design and experiments of a novel hydraulic wheel-legged robot (WLR), ” in Proc. IEEE/RSJ Int. Conf. Intell. Robots Syst., 2018, pp. 3292–3297.
[5] X. Li, H. Zhou, S. Zhang, H. Feng, and Y. Fu, “WLR-II, a hose-less hydraulic wheel-legged robot, ” in Proc. IEEE/RSJ Int. Conf. Intell. Robots Syst., 2019, pp. 4339–4346.
[6] H. Zhou, X. Li, H. Feng, J. Li, S. Zhang, and Y. Fu, “Model decoupling and control of the wheeled humanoid robot moving in sagittal plane, ” in Proc. Int. Conf. Hum. Robot., 2019, pp. 1–6.
[7] Jemin Hwangbo etal., Learning agile and dynamic motor skills for legged robots.Sci. Robot.4, eaau5872(2019).DOI: 10.1126/scirobotics.aau5872
[8] Guan, Y.H. (2023). [RM2023] Open Source of Balanced Infantry Control System: Shanghai Jiaotong University - Yunhan Jiaolong.. Retrieved from https: //bbs.robomaster.com/article/9430
[9] H. Chen, B. Wang, Z. Hong, C. Shen, P. M. Wensing and W. Zhang, "Underactuated Motion Planning and Control for Jumping With Wheeled-Bipedal Robots, " in IEEE Robotics and Automation Letters, vol. 6, no. 2, pp. 747-754, April 2021, doi: 10.1109/LRA.2020.3047787.